Efficient protons acceleration by a petawatt Laguerre–Gaussian laser from a concave micro-structured target

Song-Tao Li(李松涛)[1,2], Wan-Xin Dong(董万鑫)[1], Meng Liu(刘梦)[1,2,†], and Wei-Min Wang(王伟民)[3,‡]

[1] *North China Electric Power University (Baoding), Baoding* 071003, *China*
[2] *Hebei Key Laboratory of Physics and Energy Technology, Baoding* 071003, *China*
[3] *State Key Laboratory of Dark Matter Physics, Key Laboratory for Laser Plasmas (MOE), School of Physics and Astronomy, Shanghai Jiao Tong University, Shanghai* 200240, *China*

(Received 24 September 2025; revised manuscript received 26 January 2026; accepted manuscript online 10 February 2026)

Laser-driven ion sources have the advantages of compact size, high density, and short bunch duration over conventional acceleration. Nevertheless, it remains challenging to simultaneously enhance the yield and quality of laser-driven ion beams for applications such as tumor therapy. Here we propose a scheme to address this challenge by using a concave micro-structured (CMS) target irradiated by multi-petawatt Laguerre–Gaussian (LG) lasers. During the interaction of the LG laser with the CMS target, a longitudinal charge-separation field with a broad dual-peak structure is excited, and it maintains this shape with a large amplitude for dozens of laser cycles. This special distribution can simultaneously accelerate and converge the ions within the laser spot region. Particle-in-cell simulations demonstrate that, under irradiation by LG lasers with peak intensities ranging from 10^{20} W/cm^2 to 10^{22} W/cm^2, CMS hydrocarbon targets double the high-energy proton yield compared to planar finite-sized targets while maintaining high collimation. Typically, a quasi-monoenergetic proton beam with a peak energy of ~ 72.3 MeV and a divergence angle of less than 10° can be generated using the CMS target. This work could provide a reference for high-quality ion beam generation with recently available petawatt (PW)-class LG laser systems.

Keywords: Laguerre–Gaussian laser, micro-structured target, laser-driven ion acceleration, particle-in-cell simulations

PACS: 52.38.Kd, 52.65.Rr, 41.75.Jv

DOI: 10.1088/1674-1056/ae43c8 **CSTR:** 32038.14.CPB.ae43c8

1. Introduction

Driven by the rapid development of ultra-intense, ultrashort-pulse laser technology,[1] focused laser intensities exceeding 10^{22} W/cm^2 have been achieved in the laboratory.[2–4] The study of MeV–GeV ion beams generated by ultra-high-intensity lasers has become a topic of growing interest.[5–7] This stems from the unique characteristics of laser-driven ion beams, including low transverse emittance, ultrashort durations and high current densities,[6,7] which offer significant potential for applications in cancer treatment,[8–10] proton imaging,[11] fast ignition in inertial confinement fusion (ICF),[12–14] and neutron source generation.[15,16] One crucial requirement for many of these applications is the reduction of beam divergence to enhance beam brilliance and energy.

Since 2000, with advances in laser technology and improvements in target fabrication techniques, researchers have carried out extensive theoretical and experimental work aimed at enhancing ion beam quality.[17–26] These efforts have elucidated several crucial physical mechanisms underlying ion acceleration. When high-intensity lasers irradiate solid targets, a MeV-range proton beam can be generated along the target rear normal.[18,23] This mechanism, known as target normal sheath acceleration,[27] is currently the most extensively studied and relatively stable method in experiments. However, the ion energy spectrum obtained using this method is usually broad and continuous, and the proton beam emission angle is generally large (usually over 10°).[17,28] As a result, these particle sources are unsuitable for ion accelerator applications. Recently, radiation pressure acceleration (RPA) using circularly polarized (CP) lasers has emerged as one of the most promising schemes for obtaining high-energy monoenergetic ion beams.[29–33] However, various effects in multidimensional geometries, such as the finite spot size,[34] transverse expansion,[35] and transverse instabilities[32,36–39] caused by laser pressure on the dense target, can disrupt the laser-target matching relationship and terminate RPA. As a result, the accelerating ion beam undergoes RPA breakdown, leading to a significant reduction in laser-to-ion conversion efficiency.

There is a need to develop new methods to improve ion beam quality for upcoming high-repetition-rate petawatt (PW) laser systems. Recently, at the Shanghai Ultra-Intense Ultra-Short Laser Facility (SULF), the intensity of the ultra-intense vortex laser (Laguerre–Gaussian laser)[40,41] was increased to

†Corresponding author. E-mail: liumeng@ncepu.edu.cn
‡Corresponding author. E-mail: weiminwang1@sjtu.edu.cn

© 2026 Chinese Physical Society and IOP Publishing Ltd. All rights, including for text and data mining, AI training, and similar technologies, are reserved.

CPB Online In Press

the order of 3×10^{20} W/cm^2.[42] The relativistic Laguerre–Gaussian (LG) laser, with its intrinsic hollow intensity distribution, is expected to enable proton focusing and collimation in a simple manner.[42] However, the efficient generation of quasi-monoenergetic proton beams driven by LG-mode lasers has not been extensively investigated.[43,44]

In this paper, we propose a novel method to enhance radiation pressure ion acceleration using multi-petawatt LG lasers and a concave micro-structured (CMS) target. The target surface is shaped into a parabolic profile, as shown schematically in Fig. 1. At the beginning of the laser-plasma interaction, the conditions for hole-boring radiation pressure acceleration (HB-RPA)[45] are satisfied because the target thickness increases gradually from the center to the edge, optimally matching the characteristic donut-like intensity distribution of the LG vortex mode. This results in the preferential acceleration of most protons within the region of $r\sim w_0/\sqrt{2}$, forming a ring-shaped structure that propagates along the laser direction. Particle-in-cell (PIC) simulations demonstrate that CMS targets can stably generate quasi-monoenergetic proton beams and enhance the yield of high-energy protons when driven by circularly polarized LG lasers with intensities ranging from 10^{20} W/cm^2 to 10^{22} W/cm^2. Additionally, the inward ponderomotive force of LG lasers effectively controls the lateral divergence of high-energy protons. In contrast, a planar finite-sized target driven by an LG laser typically produces broad energy spectra with a low yield of high-energy protons.

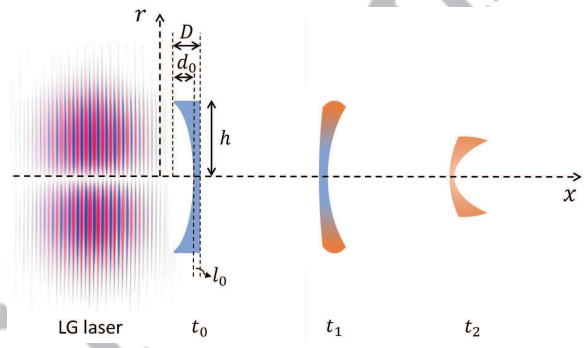


Fig. 1. Physical model of the interaction between a LG laser and a concave micro-structured target. Here, d_0 is the depth of the target front surface, h is the finite radius of the target, and l_0 is the target thickness at $r=0$. Thus, the target thickness is given by $D(r)=d+l_0$.

2. Theoretical method

To obtain an ultra-relativistic-intensity LG laser, a spiral phase plate with a spirally varying thickness should be used. The vortex laser with ultra-relativistic intensity in the experiment mentioned above is usually obtained by the incoherent superposition of several low-order LG lasers.[20,46–48] Therefore, in this paper, we adopted an LG pulse with azimuthal quantum number $l=1$ and radial quantum number $p=0$. The electric field profile of the LG laser is

$$E_{\mathrm{LG},01}(r,\phi,t) = E_{\mathrm{peak}}\left(\frac{\sqrt{2}r}{w_0}\right)\exp\left[-\frac{r^2}{w_0^2}\right] \times\exp\left[\mathrm{i}(l\phi-\omega t)\right]\hat{e}_{\mathrm{c}}. \quad (1)$$

Here, E_{peak} is the peak value of the electric field normalized to $E_0=2\pi m_{\mathrm{e}}c^2/(e\lambda)$, e is the electron charge, m_{e} is the electron mass, and w_0 is the laser focal spot radius. $\hat{e_{\mathrm{c}}}$ represents the unit vector of circular polarization. For example, right-handed circular polarization is denoted by $\hat{e_-}=(\hat{x}-\mathrm{i}\hat{y})/\sqrt{2}$, while left-handed circular polarization is denoted by $\hat{e_+}=(\hat{x}+\mathrm{i}\hat{y})/\sqrt{2}$. In addition, each photon in the LG laser carries an orbital angular momentum (OAM) of $l\hbar$. Thus, each photon carries a total angular momentum of $(l\mp1)\hbar$. In this paper, the angular momentum of the photons is assumed to be zero, which ensures that the LG laser has an inward ponderomotive force and does not transfer its angular momentum to the protons.[47]

Assuming that the LG laser duration is τ, its longitudinal Gaussian envelope is given by

$$E_{\mathrm{LG},01}(r,\phi,t) = E_{\mathrm{peak}}\left(\frac{\sqrt{2}r}{w_0}\right)\exp\left[-\frac{r^2}{w_0^2}\right]\exp\left[-\frac{t^2}{\tau^2}\right] \times\left[\cos(\omega t-\phi)\hat{x}+\sin(\omega t-\phi)\hat{y}\right]. \quad (2)$$

The ponderomotive force F_{p} is determined by the gradient of the squared magnitude of the laser electric field, that is

$$F_{\mathrm{p}}=-\frac{e^2}{4m_{\mathrm{e}}\omega^2}\nabla\mid E\mid^2. \quad (3)$$

The radial ponderomotive force generated by the LG laser is expressed as follows:

$$F_{\mathrm{p}}(r)=\frac{e^2E_{\mathrm{peak}}^2r}{2m_{\mathrm{e}}\omega^2w_0^2}\exp\left(-\frac{2r^2}{w_0^2}\right)\exp\left(-\frac{2t^2}{\tau^2}\right)\left(1-\frac{2r^2}{w_0^2}\right), \quad (4)$$

when $r<w_0/\sqrt{2}$, the ponderomotive force is inward, whereas it is outward when $r>w_0/\sqrt{2}$. Thus, in the region $r<w_0/\sqrt{2}$, the ponderomotive force pushes the electrons forward while simultaneously compressing them toward the laser propagation axis.

Efficient radiation pressure acceleration requires a large number of ions to be accelerated to a uniform kinetic energy ε_{i}, given by $\varepsilon_{\mathrm{i}}=m_{\mathrm{i}}c^2\Pi^2/[2(\Pi+1)]$. This condition can be achieved by keeping the dimensionless parameter Π constant,[45,49] where $\Pi=2m_{\mathrm{e}}n_{\mathrm{c}}{a_0}^2\tau c/(\Sigma_{\mathrm{i}}m_{\mathrm{i}}n_{\mathrm{i}}L)$. Previous studies[45,49,50] have demonstrated that high-flux, high-energy ion beams can be produced via RPA by tailoring micron-scale solid targets to match the target's areal density ($n_{\mathrm{i}}L$) distribution to the spatial profile of the laser intensity. For this purpose, we designed a concave micro-structured (CMS) target featuring a parabolic profile, as shown in Fig. 1. Its surface profile is given by

$$d=d_0(1-r^2/2R_{\mathrm{c}}^2). \quad (5)$$

Chin. Phys. B Online First

Here, d_0 is the depth of the target front surface, R_c is the radius of curvature, and the finite radius of the target is $h = \sqrt{2}R_c$. Thus, the target thickness is $D(r) = (d_0 - d) + l_0$, where l_0 is the target thickness at $r = 0$. The corresponding target areal density, $n_e \times D(r)$, increases radially from $n_e l_0$ to $n_e D(r = w_0/\sqrt{2})$, matching the hollow distribution of the normalized laser amplitude $a_0 = |eE(r)/(\omega m_e c)|$. As a result, this CMS target allows more ions to be accelerated to the uniform energy determined by a constant parameter Π.

3. Results and discussion

To achieve efficient ion acceleration using a circularly polarized LG laser with a micro-structured target, we carried out a series of two-dimensional (2D) particle-in-cell (PIC) simulations using the code EPOCH.[51] The CP laser has a wavelength of $\lambda = 1$ μm and a corresponding laser cycle of $T_0 = \lambda/c$. The amplitude profile of the LG laser is determined by Eq. (2). The normalized amplitude of the CP laser is $a_0 = [I_0\lambda^2/(2.74 \times 10^{18})]^{1/2}$. In typical simulations, a 30 fs laser has an amplitude a_0 ranging from 10 to 200 and a beam waist of $w_0 = 8\lambda$. The laser wavefront reaches the vacuum-target interface at $x = 10$ at $t = 0$. The target is composed of carbon ions C^{6+}, protons H^+, and electrons e^-. The uniform plasma density is $n_e = 200n_c$, where $n_c = m_e\omega^2/(4\pi e^2)$ is the critical density and ω is the laser angular frequency. The front surface of the concave micro-structured (CMS) target is defined by Eq. (5), with a finite radius of $h = \sqrt{2}R_c$ and $R_c = 5\lambda$. In each simulation, a simulation box of dimensions $x \times y = 70\lambda \times 40\lambda$ is divided into 11200×4800 cells, with 100 macroparticles per cell in the foil region. For comparison, a planar target with the same radial size h is irradiated by an LG laser. Its thickness is L, and the corresponding areal density $n_e \times L$ is set equal to that of the CMS target, i.e., $n_e \times L = n_e \times D(r)$. This ensures that the ions can be accelerated to the same energy under the radiation pressure of an LG laser with the same a_0.[6,32,52]

Simulation results show that quasi-monoenergetic proton beams are generated efficiently when LG lasers with intensities of 1.71×10^{21}–6.16×10^{22} W·cm^{-2} interact with CMS targets. As shown in Fig. 2(a), the CMS target driven by the LG laser exhibits a laser-to-energetic-proton energy conversion efficiency η that increases approximately linearly from 3.1% to 6.8% as the laser amplitude a_0 rises from 25 to 100. For $a_0 \geq 100$, the efficiency saturates at around 6.8%. However, the conversion efficiency η for the planar target is significantly lower than that for the CMS target. For example, at $a_0 = 50$, the energy conversion efficiency is $\eta \simeq 5.1\%$ for the CMS target, whereas it is only $\eta \simeq 2.9\%$ for the planar target. Moreover, for the CMS target driven by the LG laser, the peak proton energy ε_{peak} increases from 27 MeV to 430 MeV as a_0 rises from 25 to 150, as shown by the black stars in Fig. 2(a). Concurrently, the proton yield in the quasi-monoenergetic proton beam also increases substantially, as indicated by the blue rectangles in Fig. 2(b). In contrast, no quasi-monoenergetic peak is generated, or the peak is much lower, for planar targets at $a_0 \leq 75$. Furthermore, the total number of energetic protons produced by the CMS target is approximately twice that produced by the planar target over the range $25 \leq a_0 \leq 100$.

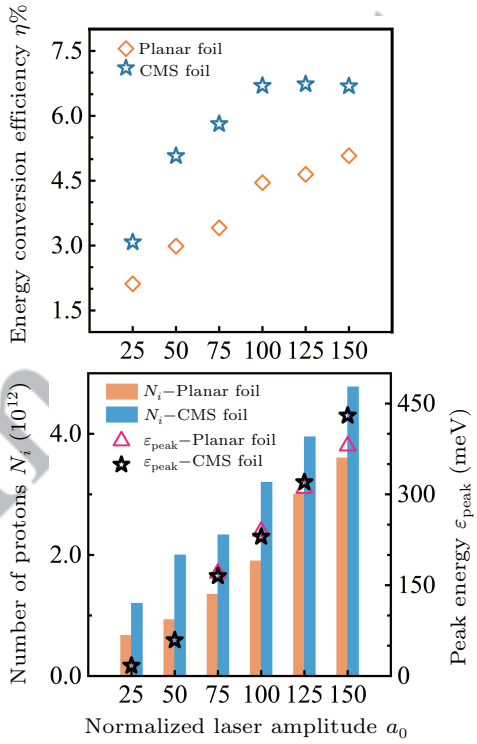


Fig. 2. (a) The energy conversion efficiency from the laser to energetic protons as a function of the laser amplitude a_0, where blue stars and orange stars correspond to CMS targets and planar targets, respectively. (b) The peak energies ε_{peak} of the quasi-monoenergetic proton beams are indicated by black stars and red triangles for CMS targets and planar targets, respectively. The blue and orange rectangles represent the numbers of protons in the corresponding quasi-monoenergetic proton beams. The corresponding parameters for the circularly polarized LG laser and targets are ($a_0 = 25$, $L = 0.08\lambda$, $d_0 = 0.1\lambda$, $l_0 = 0.05\lambda$); ($a_0 = 50$, $L = 0.16\lambda$, $d_0 = 0.2\lambda$, $l_0 = 0.09\lambda$); ($a_0 = 75$, $L = 0.19\lambda$, $d_0 = 0.2\lambda$, $l_0 = 0.12\lambda$); ($a_0 = 100$, $L = 0.26\lambda$, $d_0 = 0.30\lambda$, $l_0 = 0.16\lambda$); ($a_0 = 125$, $L = 0.32\lambda$, $d_0 = 0.35\lambda$, $l_0 = 0.20\lambda$); ($a_0 = 150$, $L = 0.38\lambda$, $d_0 = 0.40\lambda$, $l_0 = 0.25\lambda$).

To further analyze proton acceleration driven by the LG laser with either a CMS target or a planar target, we show the distributions of the longitudinal charge-separation field E_x and the electron density in Fig. 3. At the early stage ($t = 20T_0$) of the interaction between the LG laser and the target, as shown in Figs. 3(a) and 3(b), E_x exhibits an inward, bowl-shaped profile with a large amplitude. The black curve in Fig. 3(e), which shows the corresponding electric field profile in Fig. 3(a), exhibits two peaks of $7.2E_0$ around $|y| \simeq 4.80\lambda$. This can be attributed to the hollow intensity distribution of the LG laser, whose peak intensity occurs at $|y| = w_0/\sqrt{2} \simeq 5.56\lambda$ and which provides a ponderomotive force described by Eq. (4). The force is inward when $y \leq w_0/\sqrt{2}$ and outward when $y \geq w_0/\sqrt{2}$. Thus, as shown in Fig. 3(c), the target electrons

CPB Online Ip

are pushed forward by the longitudinal component of the ponderomotive force and simultaneously compressed toward the laser propagation axis by its inward component in the region where $y \leq w_0/\sqrt{2}$. As a result, the induced charge-separation field exhibits a two-peak structure with a large amplitude.

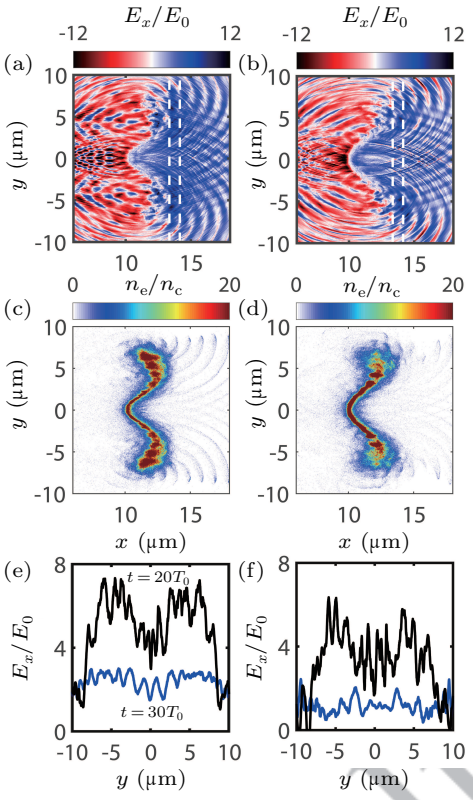


Fig. 3. Spatial distributions of the longitudinal electric field E_x and the electron density n_e for a LG laser irradiating a CMS target (a)–(c) and a planar target (d)–(f). The longitudinal electric field E_x, averaged over the same longitudinal region (the white dotted-line regions in (a) and (d)), is also plotted as black curves at $t = 20T_0$ and blue curves at $t = 30T_0$ in (e) and (f). The normalized laser amplitude is $a_0 = 50$, the planar target thickness is $L = 0.16\lambda$, and the CMS target parameters satisfy $d_0 + l_0 = (0.2 + 0.09)\lambda$.

Furthermore, the charge-separation field maintains its distinctive shape with a large amplitude for a longer time in the CMS target than in the planar target. As shown by the blue curve in Fig. 3(e), during the propagation of the LG laser through the CMS target, the peak electric field E_x decreases from $7.2E_0$ to $3.0E_0$ over 10 laser cycles. However, for the planar target, the peak E_x drops dramatically to $1.5E_0$, as indicated by the blue curve in Fig. 3(f). In addition, the width of the region where E_x exceeds $4.0E_0$ reaches $\Delta y = 6.7\lambda$ for the CMS target, which is twice that for the planar target. This results from the target design based on Eq. (5), in which the target thickness increases gradually from $D = 0.09\lambda$ at $y = 0$ to $D = 0.22\lambda$ at $y = w_0/\sqrt{2} = 5.56\lambda$. Correspondingly, the amplitude of the LG laser increases from the center toward $|y| = 5.56\lambda$, eventually reaching its peak value of $a_0 = 50$. These matching conditions enhance the ponderomotive compression and forward acceleration of more electrons around $|y| \simeq 5.56\lambda$, as evidenced by the electron density distributions in Figs. 3(c) and 3(d). As a result, the increased electron accumulation forms an arch-shaped profile and sustains the induced charge-separation field E_x, which has a broad, dual-peak structure, for a longer time.

Consequently, the charge-separation field excited in the CMS target, with its two effective peak regions, can cause a large number of accelerated protons to accumulate near the region of high laser intensity where $y \simeq w_0/\sqrt{2}$, as shown by the proton density distributions in Figs. 4(a)–4(c). The corresponding phase-space distribution in Fig. 4(e) indicates that the longitudinal momentum p_x of these simultaneously accelerated and accumulated protons exceeds $0.4m_ic$ under the hole-boring radiation pressure acceleration mechanism.[53,54] In contrast, for the planar target, only a small number of protons are accelerated and converge noticeably around the laser propagation axis ($y = 0$) because of the charge-separation field's narrow profile and low amplitude, as can be seen from the proton density distributions in Figs. 4(b)–4(d). Thus, the number of protons with a longitudinal momentum exceeding $0.4m_ic$ in Fig. 4(f) is lower than that for the CMS target.

In addition, Figs. 5(a) and 5(b) compare the divergence angles of energetic protons. The results show that the quasi-monoenergetic proton beam produced by the CMS target has a small divergence angle of about 9.6° within the energy range of 50–150 MeV, whereas that for the planar target is about 54.4°. Here, we calculate the proton angle

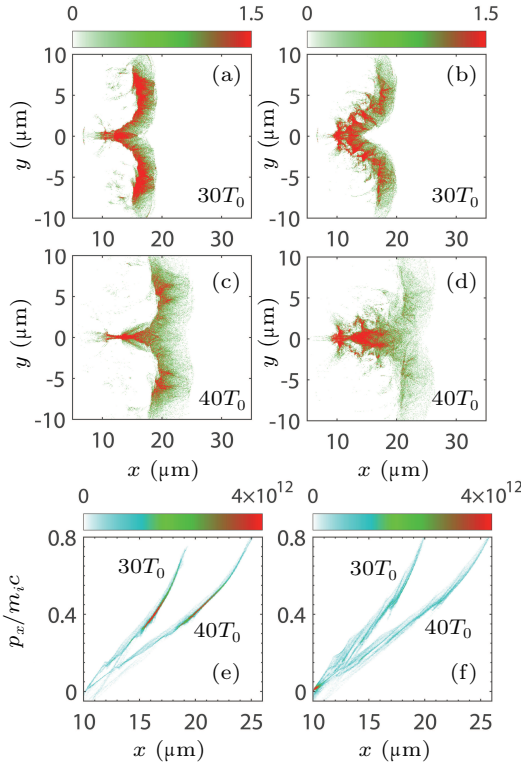


Fig. 4. Proton density distributions for a LG laser irradiating a CMS target (a)–(c) and a planar target (d)–(f). Panels (e) and (f) show the corresponding proton phase-space distributions (x–p_x). The laser and target parameters are the same as those in Fig. 3.

CPB Online In-Press

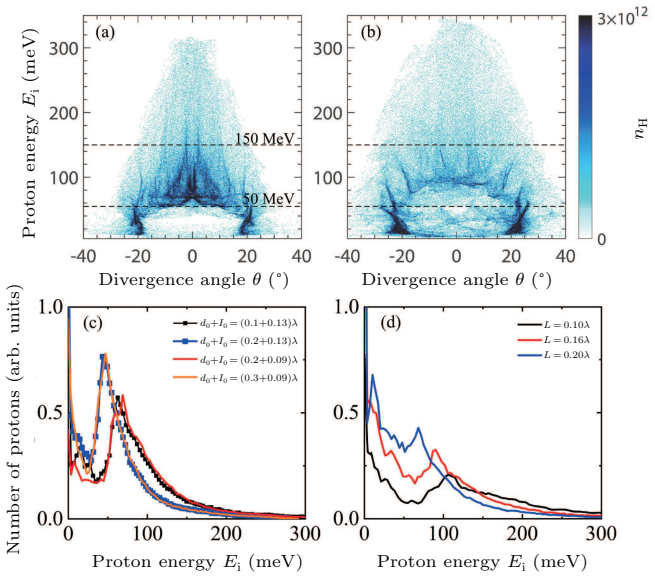


Fig. 5. Number distributions of energetic protons as functions of the divergence angle and energy for the CMS target (a) and the planar target (b). Panels (c)–(d) show the proton energy spectra for different target parameters.

($\theta_i = \arctan(p_y/p_x)$) and then obtain the count N_θ as a function of θ within the energy range of 50–150 MeV. The divergence angle is defined as the full width at half maximum of the $\theta - N_\theta$ distribution for each target. Moreover, Fig. 5(d) indicates that the accelerated protons from planar targets of different thicknesses L exhibit broad spectra or a low number of high-energy protons.[24,55,56] In contrast, the CMS target significantly enhances the yield of energetic protons and produces a distinct energy peak at 72.3 MeV, as shown in Fig. 5(c) for $(d_0, l_0) = (0.2\lambda, 0.09\lambda)$ and $(0.1\lambda, 0.13\lambda)$. The corresponding proton energy spread is about 0.58. In addition, for the same a_0, the peak energy of accelerated protons decreases with increasing areal density, as shown in Fig. 5(c). The proton peak energy decreases from 72.3 MeV to 47.0 MeV because of the higher areal density of the CMS targets with parameters $(d_0, l_0) = (0.2\lambda, 0.13\lambda)$ and $(0.3\lambda, 0.09\lambda)$ compared with those with parameters $(d_0, l_0) = (0.1\lambda, 0.13\lambda)$ and $(0.2\lambda, 0.09\lambda)$. This trend can be understood from the expression for the kinetic energy, $\varepsilon_i = m_i c^2 \Pi^2/[2(\Pi+1)]$, where $\Pi = 2m_e n_c a_0^2 \tau c/(\Sigma_i m_i n_i L)$.[45,49]

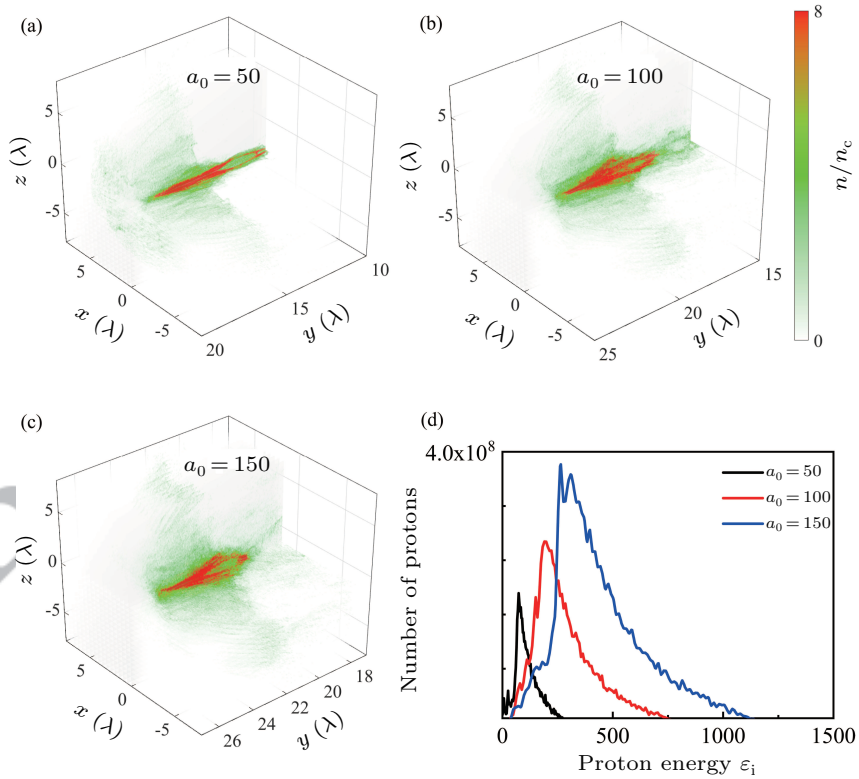


Fig. 6. Proton density distributions at $t = 30T_0$ for laser amplitudes of $a_0 = 50$ (a), $a_0 = 100$ (b), and $a_0 = 150$ (c). Panel (d) shows the corresponding proton energy spectra. The parameters of the circularly polarized LG laser and targets are ($a_0 = 50$, $d_0 = 0.25\lambda$, $l_0 = 0.1\lambda$); ($a_0 = 100$, $d_0 = 0.32\lambda$, $l_0 = 0.20\lambda$); and ($a_0 = 150$, $d_0 = 0.45\lambda$, $l_0 = 0.25\lambda$). All targets have the same radial size, $h \simeq w_0$.

We also perform 3D simulations of an LG laser with normalized amplitudes of $a_0 = 50$, 100, and 150 interacting with a CMS target. The 3D simulations use the same laser pulse and foil composition as those in the 2D simulations. A simulation box of $50\lambda \times 30\lambda \times 30\lambda$ is used, divided into $2000 \times 600 \times 600$ cells along x, y, and z, respectively. The simulation box moves along x at the speed of light, with 32 macro-particles per cell in the foil region. Figures 6(a)–6(c) show that the accelerated protons converge well and reach a peak density of $n_H \geq 8n_c$ after the LG laser interacts with the CMS targets for $t = 30\ T_0$. The corresponding energy peaks of 73 MeV, 198 MeV, and 313 MeV, as shown in Fig. 6(d), are consistent with the peak

In Press
CPR

energies obtained in the 2D simulations shown in Fig. 2(b). In addition, we use the EPOCH code to investigate the effects of strong-field quantum electrodynamics (QED) on radiation pressure acceleration (RPA).[57] The effects on proton beam quality are negligible.[55,56,58,59] For $a_0 = 150$, the energy conversion efficiency from the laser to gamma-ray photons is about 1.3%. In efficient RPA, electrons move mainly along the laser propagation direction, resulting in small QED parameters and weak QED effects.[57,59]

In addition, for the laser intensities of 10^{20}–10^{22} W/cm^2 considered in our simulations, the influence of laser prepulses should be considered. At these intensities, a pulse with an amplified spontaneous emission (ASE) contrast as low as 10^{-11} can generate a low-density preplasma in front of a solid target.[60,61] Therefore, in the 2D PIC simulations, a preplasma with an exponential density profile and a scale length L is introduced in front of the CMS target, where L varies from 0.1λ to 1λ. As shown in Fig. 7(a), distinct peaks emerge in the proton energy spectra, with the peak energy increasing from 52 MeV to 76 MeV as the preplasma scale length L increases from 0.3λ to 0.5λ. However, when L reaches 0.9λ, the peak energy shows almost no further increase. The distributions of energetic protons as functions of the divergence angle and energy for different scale lengths L are presented in Figs. 7(b)–7(d). The results show that, with a preplasma scale length of $L = 0.3\lambda$ in front of the CMS target, the yield of high-energy protons (30–150 MeV) is about 7.1×10^{11}, and the corresponding divergence angle is approximately 18°. When L increases to 0.9λ, the divergence angle grows to about 30°, indicating a deterioration in beam collimation as the preplasma length increases.

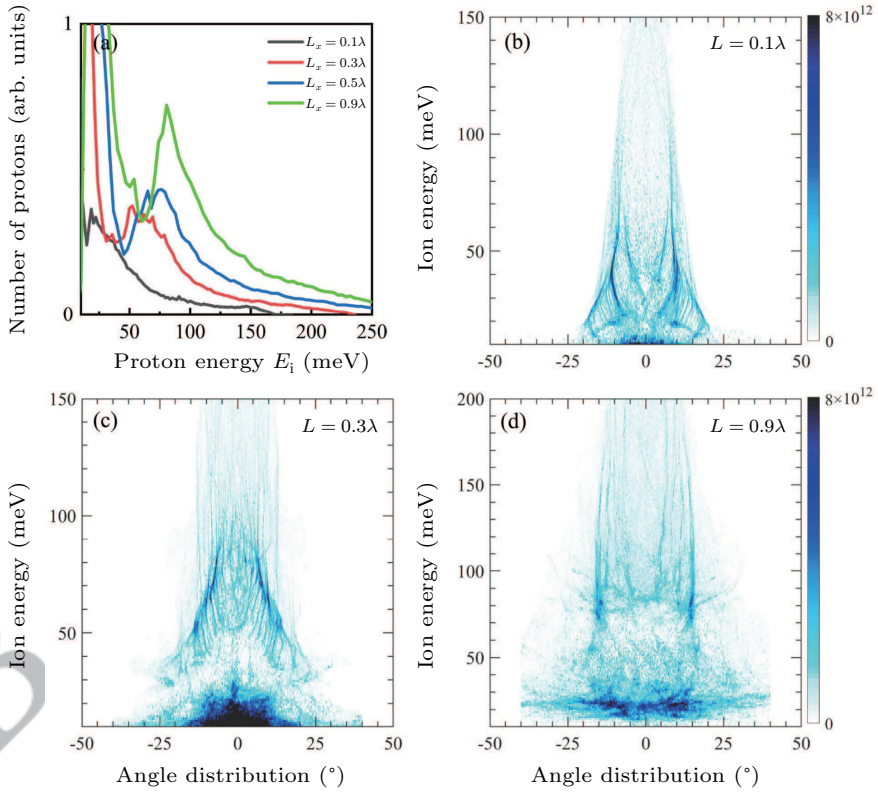


Fig. 7. (a) Proton energy spectra for different preplasma scale lengths L in front of the CMS target. (b)–(d) Number distributions of energetic protons as functions of the divergence angle for $L = 0.1\lambda$, 0.3λ, and 0.5λ, respectively. The normalized laser amplitude is $a_0 = 50$.

4. Conclusion

In summary, we have investigated the generation of quasi-monoenergetic proton beams using PIC simulations and found that such beams can be efficiently generated when a concave micro-structured (CMS) target is irradiated by an LG laser with an intensity of 1.71×10^{21}–6.16×10^{22} W/cm^2. The CMS target, with a finite radius of $h \sim w_0$ and a suitably concave parabolic surface, maintains the longitudinal charge-separation field, which has a characteristic inward, bowl-shaped profile with dual peaks for dozens of laser periods. The protons are then efficiently accelerated and accumulated by this electrostatic field. In this way, a quasi-monoenergetic proton beam with low divergence is generated, and the total proton number is increased. In contrast, when a planar finite-size target is used, the generated proton beam has a broader energy spectrum or deviates from a monoenergetic distribution, even when the same LG laser is used. It is worth pointing out that this work could provide a reference for efficient ion acceleration experiments with PW-class laser systems that have recently become available.

Acknowledgments

Project supported by the National Natural Science Foundation of China (Grant No. 12205366), the Shanghai Municipal Science and Technology Major Project and the Hydrogen-Boron Fusion Research Fund of Beijing ENN Fusion Energy Technology Co., Ltd. (Grant No. 2026ENNHB01-011), the Fundamental Research Funds for the Central Universities and the Research Funds of Shanghai Jiao Tong University (Grant No. WH220207203), the Fundamental Research Funds for the Central Universities (Grant No. 2025MS181), and the State Grid Science and Technology Project (Grant No. kjgw2025-004).

References

[1] Strickland D and Mourou G 1985 *Opt. Commun.* **55** 447
[2] Yanovsky V, Chvykov V, Kalinchenko G, Rousseau P, Planchon T, Matsuoka T, Maksimchuk A, Nees J, Cheriaux G, Mourou G and Krushelnick K 2008 *Opt. Express* **16** 2109
[3] Yoon J W, Kim Y G, Choi I W, Sung J H, Lee H W, Lee S K and Nam C H 2021 *Optica* **8** 630
[4] Cernaianu M O, Ghenuche P, Rotaru F, *et al.* 2025 *Matter Radiat. Extremes* **10** 027204
[5] Daido H, Nishiuchi M and Pirozhkov A S 2012 *Rep. Prog. Phys.* **75** 056401
[6] Macchi A, Borghesi M and Passoni M 2013 *Rev. Mod. Phys.* **85** 751
[7] Fuchs J, Antici P, d'Humières E, *et al.* 2006 *Nat. Phys.* **2** 48
[8] Linz U and Alonso J 2007 *Phys. Rev. ST Accel. Beams* **10** 094801
[9] Bulanov S V, Khoroshkov T Z, Kuznetsov V S and Pegoraro F 2002 *Phys. Lett. A* **299** 240
[10] Bulanov S V and Khoroshkov V S 2002 *Plasma Phys. Rep.* **28** 453
[11] Borghesi M, Campbell D H, Schiavi A, Haines M G, Willi O, MacKinnon A J, Patel P, Gizzi L A, Galimberti M, Clarke R J, Pegoraro F, Ruhl H and Bulanov S 2002 *Phys. Plasmas* **9** 2214
[12] Fernández J C, Honrubia J J, Albright B J, Flippo K A, Gautier D C, Hegelich B M, Schmitt M J, Temporal M and Yin L 2009 *Nucl. Fusion* **49** 065004
[13] Tabak M, Hammer J, Glinsky M E, Kruer W L, Wilks S C, Woodworth J, Campbell E M, Perry M D and Mason R J 1994 *Phys. Plasmas* **1** 1626
[14] Naumova N, Schlegel T, Tikhonchuk V T, Labaune C, Sokolov I V and Mourou G 2009 *Phys. Rev. Lett.* **102** 025002
[15] Kar S, Green A, Ahmed H, *et al.* 2016 *New J. Phys.* **18** 053002
[16] Roth M, Cowan T E, Key M H, *et al.* 2001 *Phys. Rev. Lett.* **86** 436
[17] Snavely R A, Key M H, Hatchett S P, *et al.* 2000 *Phys. Rev. Lett.* **85** 2945
[18] Wagner F, Deppert O, Brabetz C, Fiala P, Kleinschmidt A, Poth P, Schanz V A, Tebartz A, Zielbauer B, Roth M, Stöhlker T and Bagnoud V 2016 *Phys. Rev. Lett.* **116** 205002
[19] Dover N P, Nishiuchi M, Sakaki H, *et al.* 2020 *Phys. Rev. Lett.* **124** 084802
[20] Ji L L, Shen B F, Zhang X M, Wang F C, Jin Z Y, Li X M, Wen M and Cary J R 2008 *Phys. Rev. Lett.* **101** 164802
[21] Haberberger D, Tochitsky S, Fiuza F, Gong C, Fonseca R A, Silva L O, Mori W B and Joshi C 2012 *Nat. Phys.* **8** 95
[22] Li A X, Qin C Y, Zhang H, *et al.* 2022 *High Power Laser Sci. Eng.* **10** e26
[23] Higginson A, Gray R J, King M, *et al.* 2018 *Nat. Commun.* **9** 724
[24] Macchi A, Veghini S, Liseykina T V and Pegoraro F 2010 *New J. Phys.* **12** 045013
[25] Bulanov S S, Esarey E, Schroeder C B, Bulanov S V, Esirkepov T Zh, Kando M, Pegoraro F and Leemans W P 2015 *Phys. Rev. Lett.* **114** 105003
[26] Marco S C D, Mondal S, Margarone D and Kahaly S 2023 *Matter Radiat. Extremes* **8** 054001
[27] Wilks S C, Langdon A B, Cowan T E, Roth M, Singh M, Hatchett S, Key M H, Pennington D, MacKinnon A and Snavely R A 2001 *Phys. Plasmas* **8** 542
[28] Zepf M, Clark E L, Beg F N, Clarke R J, Dangor A E, Gopal A, Krushelnick K, Norreys P A, Tatarakis M, Wagner U and Wei M S 2003 *Phys. Rev. Lett.* **90** 064801
[29] Esirkepov T, Borghesi M, Bulanov S V, Mourou G and Tajima T 2004 *Phys. Rev. Lett.* **92** 175003
[30] Macchi A, Cattani F, Liseykina T V and Cornolti F 2005 *Phys. Rev. Lett.* **94** 165003
[31] Robinson A P L, Zepf M, Kar S, Evans R G and Bellei C 2008 *New J. Phys.* **10** 013021
[32] Yan X Q, Lin C, Sheng Z M, Sheng Z Y, Guo Z Y, Liu B C, Lu Y R, Fang J X and Chen J E 2008 *Phys. Rev. Lett.* **100** 135003
[33] Qiao B, Zepf M, Borghesi M, Dromey B, Geissler M, Karmakar A and Gibbon P 2010 *Phys. Rev. Lett.* **105** 155002
[34] Dollar F, Zulick C, Thomas A G R, Chvykov V, Davis J, Kalinchenko G, Matsuoka T, McGuffey C, Petrov G M, Willingale L, Yanovsky V, Maksimchuk A and Krushelnick K 2012 *Phys. Rev. Lett.* **108** 175005
[35] Yan X Q, Wu H C, Sheng Z M, Chen J E and Meyer-ter-Vehn J 2009 *Phys. Rev. Lett.* **103** 135001
[36] Shen X F, Qiao B, Zhang H, Kar S, Zhou C T, Chang H X, Borghesi M and He X T 2017 *Phys. Rev. Lett.* **118** 204802
[37] Palmer C A J, Schreiber J, Nagel S R, *et al.* 2012 *Phys. Rev. Lett.* **108** 225002
[38] Wan Y, Andriyash I A, Lu W, Mori W B and Malka V 2020 *Phys. Rev. Lett.* **125** 104801
[39] Paradkar B S and Krishnagopal S 2016 *Phys. Rev. E* **93** 023203
[40] Wang W P, Jiang C, Shen B F, Yuan F, Gan Z M, Zhang H, Zhai S H and Xu Z Z 2019 *Phys. Rev. Lett.* **122** 024801
[41] Wang W P, Jiang C, Dong H, Lu X M, Li J F, Xu R J, Sun Y J, Yu L H, Guo Z, Liang X Y, Leng Y X, Li R X and Xu Z Z 2020 *Phys. Rev. Lett.* **125** 034801
[42] Wang W P, Sun X Y, Sun F Y, Lv Z X, Glize K, Shi Z Y, Xu Y, Zhang Z X, Wu F X, Hu J B, Qian J Y, Zhu J C, Liang X Y, Leng Y X, Li R X and Xu Z Z 2025 *Commun. Phys.* **8** 281
[43] Wang W P, Dong H, Shi Z Y, Leng Y X, Li R X and Xu Z Z 2022 *Appl. Phys. Lett.* **121** 214102
[44] Pae K H, Song H, Ryu C M, Nam C H and Kim C M 2020 *Plasma Phys. Control. Fusion* **62** 055009
[45] Weng S M, Liu M, Sheng Z M, Murakami M, Chen M, Yu L L and Zhang J 2016 *Sci. Rep.* **6** 22150
[46] Wang W P, Shen B F, Zhang X M, Zhang L G, Shi Y and Xu Z Z 2015 *Sci. Rep.* **5** 8274
[47] Gao J X, Liu M and Wang W M 2023 *Chin. Phys. B* **32** 105202
[48] Zhang X M, Shen B F, Zhang L G, Xu J C, Wang X F, Wang W P, Yi L Q and Shi Y 2014 *New J. Phys.* **16** 123051
[49] Liu M, Weng S M, Wang H C, Chen M, Zhao Q, Sheng Z M, He M Q, Li Y T and Zhang J 2018 *Phys. Plasmas* **25** 063103
[50] Wang T, Khudik V and Shvets G 2021 *Phys. Rev. Lett.* **126** 024801
[51] Arber T D, Bennett K, Brady C S, Douglas A L, Ramsay M G, Sircombe N J, Gillies P, Evans R G, Schmitz H, Bell A R and Ridgers C P 2015 *Plasma Phys. Control. Fusion* **57** 113001
[52] Yu T P, Pukhov A, Shvets G and Chen M 2010 *Phys. Rev. Lett.* **105** 065002
[53] Robinson A P L, Kwon D H and Lancaster K 2009 *Plasma Phys. Control. Fusion* **51** 095006
[54] Weng S M, Murakami M, Mulser P and Sheng Z M 2012 *New J. Phys.* **14** 063026
[55] Liu M, Gao J X, Wang W M and Li Y T 2022 *Appl. Sci.* **12** 2924
[56] Liu M, Wang W M and Li Y T 2024 *Phys. Rev. E* **109** 015208
[57] Piazza A D, Müller C, Hatsagortsyan K Z and Keitel C H 2012 *Rev. Mod. Phys.* **84** 1177
[58] Ridgers C P, Brady C S, Duclous R, Kirk J G, Bennett K, Arber T D, Robinson A P L and Bell A R 2012 *Phys. Rev. Lett.* **108** 165006
[59] Tamburini M, Pegoraro F, Piazza A Di, Keitel C H and Macchi A 2010 *New J. Phys.* **12** 123005
[60] Dromey B, Kar S, Zepf M and Foster P 2004 *Rev. Sci. Instrum.* **75** 645
[61] Lundh O, Lindau F, Persson A, Wahlstrom C G and Batani D 2007 *Phys. Rev. E* **76** 026404

CPB Online First